http://dx.doi.org/10.1016/j.jallcom.2019.01.334

Mechanisms of DRX nucleation with grain boundary bulging and subgrain rotation in hot working of nickel-based superalloys with columnar grains

Bingchao Xie [1*], Baoyun Zhang [1], Yongquan Ning [1], M.W. Fu[2]

[1] School of Materials Science and Engineering, Northwestern Polytechnical University, Xi'an 710072, P.R. China

[2] Department of Mechanical Engineering, the Hong Kong Polytechnic University, Kowloon, Hong Kong, P.R. China

CORRESPONDING AUTHOR:

(*) Dr. Bingchao Xie

Tel: +86 29 88493744

E-mail: bcx0314@163.com (Bingchao Xie)

Abstract

Thermomechanical processing of nickel-based superalloys was conducted at the temperature of 1050-1170℃ and the strain rate of 0.001-10 s^{-1} to study the hot deformation behavior and dynamic recrystallization (DRX) of the columnar structures. Electron backscattered diffraction was employed to characterize the DRX microstructure of columnar grains during thermomechanical processing. A linear relationship between the critical strain hardening rate and the critical stress was derived and validated. The critical condition for DRX was determined from corresponding peak values directly, which can be used to predict the critical condition of DRX efficiently. In addition, it was found that both discontinuous-DRX and continuous-DRX played an important role in microstructure evolution. For columnar grains, the DRX nuclei firstly occurred at the serrated grain boundaries through grain boundary bulging. Subsequently, the continuous misorientation accumulation leaded to the subgrain rotation, which accelerated the nucleation within the deformed grains. The DRX nuclei preferred to occur at grain boundaries parallel to the loading direction due to discontinuous-DRX, which leaded to the heterogeneous distribution of the new-formed fine DRX grains. The findings provide a basis for the exact control of microstructure and thereby tailoring the needed properties of nickel-based superalloys with columnar grains using hot working process.

Keywords:

Nickel-based superalloys; Columnar grains; DRX nucleation mechanism; Grain boundary bulging; Subgrain rotation.

1. Introduction

Nickel-based superalloy ingots feature three typical microstructures, viz., fine equiaxed grains, columnar grains and coarse equiaxed grains. The crystallographic differences between columnar and equiaxed grains strongly affect the microstructure evolution during hot processing [1, 2]. Accurate control of microstructure evolution is very important for optimizing the mechanical properties of turbine disc, blade, rod, etc., which are generally made of nickel-based superalloys [3-8]. It is a proven fact that dynamic recrystallization (DRX) is one of the most important mechanisms that determine the microstructure evolution of nickel-based superalloys in hot deformation [9-13].

Currently, few researches are available on microstructure evolution of nickel-based superalloys with casting structures during deformation. A cast-and-homogenized equiaxed structure was investigated by using isothermal hot compression experiments [14]. The flow behavior was predicted based on the hyperbolic-sine function, and the DRX of equiaxed grains was studied. However, there is a large portion of columnar grains in superalloys ingot. The strong texture of columnar structure is a remarkable characteristic and should not be neglected in the investigation of the microstructure evolution and optimization of the cogging process for nickel-based superalloys. Therefore, it is critically needed to study the DRX mechanism and microstructure evolution of nickel-based superalloys with columnar grains.

In present research, thermomechanical processing of nickel-based superalloys was conducted at the temperature of 1050-1170℃ and the strain rate of 0.001-10 s^{-1}. Strain hardening and dynamic softening behaviors of columnar grains were investigated. A linear relationship between the critical strain hardening rate and the critical stress was derived and validated. Furthermore, the nucleation mechanisms incorporating grain boundary bulging and

subgrain rotation were investigated deeply and systematically. The findings benefits the control of microstructures and thereby the properties of nickel-based superalloys with columnar grains.

2. Material and experiments

As-received nickel-based superalloy ingot with 80 mm in diameter and 1000 mm in length was vacuum induction melted and vacuum arc remelted. The chemical composition (wt.%) is given in Table 1. The γ` solvus temperature was 1160℃. As shown in Fig. 1(a), typical equiaxed and columnar grains was observed on the transverse section of the ingot. The entire ingot was homogenized at 1180℃ for 4 h to eliminate the eutectic γ` + γ phases and composition segregation to some extent. Then, cylindrical samples with 8 mm in diameter and 12 mm in height were machined from the columnar grain zone of the homogenized ingot. Fig. 1(b) shows the microstructure of the samples before hot deformation.

Table 1 Chemical composition of the superalloy used in this work (wt%).

Cr	Co	Mo	Al	Ti	B	C	W	Ni
16.00	14.95	3.00	2.50	5.00	0.015	0.015	1.50	Bal.

Hot deformation was then conducted using the Gleeble-1500 simulator at the temperature of 1050, 1080, 1110, 1140, 1170℃ and the strain rate of 0.001, 0.01, 0.1, 1 and 10 s^{-1}. Samples were compressed to a height reduction of 30% or 50%. Loading directions were all perpendicular to the columnar-grain direction except one sample. This sample was compressed along the columnar-grain direction to verify a special DRX behavior. Tantalum

foils with the thickness of 0.1 mm were placed between the sample and die to decrease the friction and avoid adhesion. Samples were heated up to the deformation temperature at a heating rate of 10℃/s and then held for 10 min to obtain a uniform temperature distribution. Samples were quenched immediately by water to freeze the microstructures after deformation. Optical microscopy (OM), scanning electron microscope (SEM) and electron backscatter diffraction (EBSD) were used to characterize the microstructures and DRX behavior.

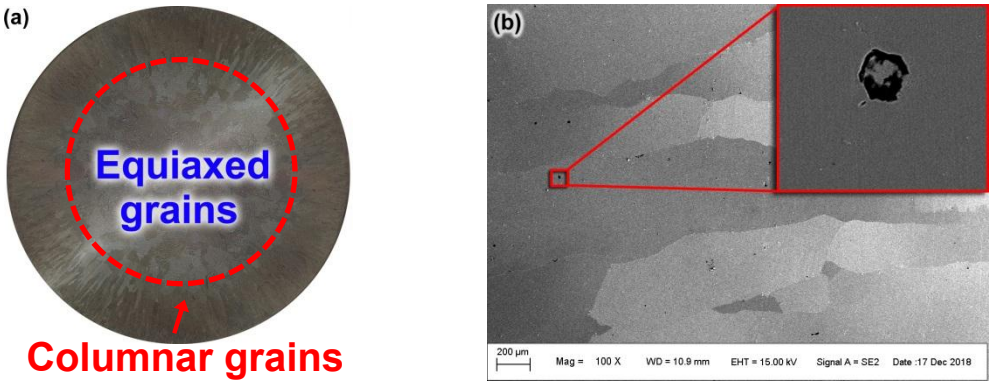

Fig. 1 (a) Macrostructure on transverse section of the ingot and (b) typical columnar grains of the cast-and-homogenized superalloy ingot.

3. Results and discussion

3.1 Deformation behavior and mechanisms

3.1.1 Flow behavior of columnar grains

Fig. 2 shows the true stress-strain curves of the nickel-based superalloy with columnar structures at the selected conditions. As shown in Fig. 2(a), the flow stress increased rapidly with strain due to the generation and multiplication of dislocations, which made dislocation slipping difficult and hence resulted in the obvious work hardening (WH) at this stage [15,

16]. Meanwhile, the dynamic recovery (DRV) caused by dislocation cross-slip and climb also took effect although it was weakened due to the relatively low stacking fault energy of this superalloy [1]. DRX occurred when the accumulated dislocation density exceeded a critical value [17] and thus gave birth to an obvious dynamic softening stage [18, 19]. The stress peak was reached when the dynamic softening cancelled out the work hardening, and then the dynamic softening dominated the subsequent stage. Finally, a relative steady regime at high strain zone was reached when a balance between dynamic softening and work hardening was achieved again. It is worth noting that each curve shown in Fig. 2 reached a gentle stress peak except for the case obtained at the temperature of 1140℃ and the strain rate of $10s^{-1}$, which was different from that of the nickel-based superalloys with coarse equiaxed grains [14]. The sharp stress peak in the curve was the result of the interaction between dislocations and alloying elements which might undergo short-range ordering or precipitation [20, 21]. Two abnormal curves obtained at 1050 and 1080℃ with the strain rate of 0.01 s^{-1} were conspicuous in Fig. 2(b) for their rapid and severe softening beyond the stress peak. Localization of strain, adiabatic deformation heating and severe cracking were found to be the dominant factors that caused the phenomenon [22, 23]. Fig. 3(a) and (b) shows the microstructures of the columnar structure deformed at the lower temperature and higher strain rate, respectively. Severe cracking occurred when the samples were deformed below 1080℃ even at the strain rate of 0.001 s^{-1}, illustrating that the columnar grains of the studied superalloy should be performed above 1080℃ to avoid shearing induced poor plasticity. Moreover, specimen also cracked severely when deformed at 1170℃ with the strain rate of 10 s^{-1} although DRX occurred obviously, as shown in Fig. 3(b). Hence the deformation with the strain rate above 10 s^{-1} should also be avoided for this columnar structure.

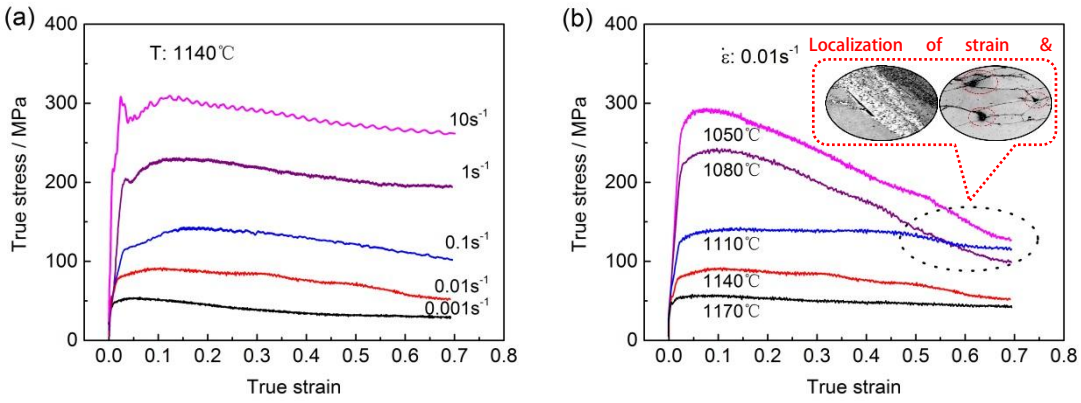

Fig. 2 True stress-strain curves of the samples compressed to ε=0.69 (a): at temperature of 1140℃ and (b): strain rate of 0.01 s^{-1}.

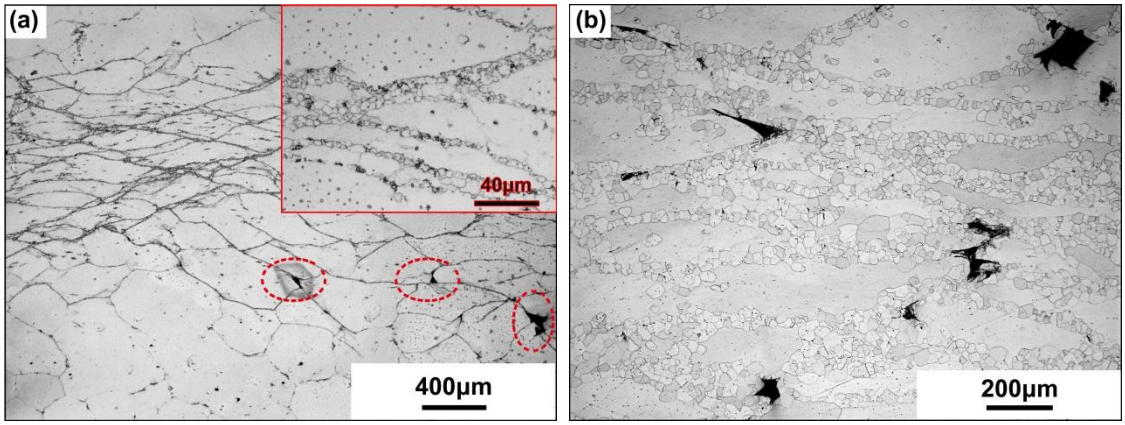

Fig. 3 Typical microstructures of the columnar structures deformed to ε=0.69 (a): at the temperature of 1080℃ with the strain rate of 0.001 s^{-1}; and (b): the temperature of 1170℃ and the strain rate of 10 s^{-1}.

3.1.2 Strain hardening and dynamic softening

Strain hardening rate $\theta = d\sigma/d\varepsilon$ has been widely employed to investigate the microstructure evolution during thermomechanical processing, especially for the dynamic softening behavior. For the curve that exhibits typical work hardening and dynamic softening

behaviors (DRV and DRX included), there are three typical stages featuring different work-hardening rates: viz., $\theta > 0$ for work-hardening stage, $\theta = 0$ for stress peak and steady stage, and $\theta < 0$ for continuous decreasing stage [24]. In order to predict the critical conditions for initiation of DRX, particular attention was paid to the strain hardening stage, i.e., the stage where flow stress ranges from zero until to peak stress. The strain hardening rate during this stage is given by:

$$\theta = d\sigma/d\varepsilon = (d\sigma/d\rho) \cdot (d\rho/d\varepsilon) \quad (1)$$

where ρ is the dislocation density. According to Tylor relation [25], the response of flow stress to dislocation density can be expressed as:

$$\sigma = \alpha GMb\sqrt{\rho} \quad (2)$$

where α denotes the Taylor constant (~0.5), G the shear modulus, M the conversion factor (~3.06) and b the magnitude of Burgers vector. By combining Eqs. (1) and (2), the strain hardening rate can be designated as:

$$\theta = d\sigma/d\varepsilon = (d\sigma/d\rho) \cdot (d\rho/d\varepsilon) = \left(\alpha GMb/(2\sqrt{\rho})\right) \cdot (d\rho/d\varepsilon) \quad (3)$$

where the first term is the response of stress to dislocation density, which is related to material parameters. While the second term represents the influence of dislocation evolution.

Dislocation multiplication and annihilation co-exist before the onset of DRX, i.e., the work-hardening and DRV stage, and compete with each other during the whole hot deformation process. Kocks-Mecking [26] model can be employed to trace the dislocation evolution during this stage for single-phase alloys as follows:

$$d\rho/d\varepsilon = k_1\sqrt{\rho} - k_2\rho \quad (4)$$

where k_1 and k_2 represent the dislocation multiplication and annihilation coefficient, respectively. With the substitution of Kocks–Mecking relation, the strain hardening rate θ_1 before the occurrence of DRX is given by:

$$\theta_1 = \alpha GMbk_1/2 - k_2/2 \cdot \sigma \quad (5)$$

When a deformation condition (deformation temperature and strain rate) is given, G and k_1 are both constants [27, 28]. Therefore, the relationship between strain hardening rate and true stress is identified as a linear relation during work-hardening and DRV stage.

While the dislocation substructures are constructed and the mean free spacing between mobile dislocations is established, the multiplication coefficient should be considered as a constant [24]. Hence, Estrin and Mecking established an equation to characterize the dislocation evolution during this stage, i.e., the stage from the occurrence of DRX to stress peak [28]:

$$d\rho/d\varepsilon = k - k_2\rho \quad (6)$$

where the constant k is determined by the mean free spacing. By combining Eqs. (2), (3) and (6), the strain hardening rate θ_2 after DRX onset until stress peak is formulated as:

$$\theta_2 = (\alpha^2 G^2 M^2 b^2 k)/(2\sigma) - k_2/2 \cdot \sigma \quad (7)$$

From the comparison between Eqs. (5) and (7), it is certain that the critical condition for DRX can be identified from the inflection point on the strain hardening rate versus true stress curve.

Using a polynomial fitting and differential method, the strain hardening rate curves of the studied material can be plotted at different deformation conditions, as shown in Fig. 4. Obvious linear decreasing regimes could be identified before the occurrence of DRX, i.e., the inflections marked with asterisks in $\theta - \sigma$ curves. It is consistent with the characteristics described by Eqs. (5) and (7). The softening of DRX results in this deviation from linear decreasing.

3.1.3 Determination of critical condition

It is worth noting that a linear relationship may exists between the critical strain hardening rate and the critical stress at a given deformation temperature (see the inflections in Fig. 4). In order to verify whether this linear relationship exists, the relation between the critical strain hardening rate and the critical stress was established based on Estrin and Mecking model [28]. In essence, it is the competition between dislocation multiplication and annihilation that dominates the work-hardening behavior. As mentioned in Eq. (6), the competition between work-hardening and dynamic softening can be expressed as:

$$d\rho/d\varepsilon = d\rho_m/d\varepsilon + d\rho_a/d\varepsilon \quad (8)$$

where the first term is the rate of dislocation multiplication and the second one is the rate of dislocation annihilation. The multiplication of dislocation density during the deformation arises from both the trapping of existing dislocations and the generation of new dislocations. During deformation, the dislocation density can be related to the true strain by [29]:

$$\varepsilon = \rho b L \quad (9)$$

where ε denotes the true strain and L the average slip distance of dislocations. The average slip distance depends on the existence of encountered obstacles, including grain boundaries, precipitates and other dislocations [25], and can be expressed as [30]:

$$1/L = 1/D + 1/d + 1/s \tag{10}$$

where D, d and s are the mean grain size, the space between the adjacent dislocations and the precipitate size, respectively. Due to the order of magnitude differences, Eq. (10) can be rewritten as:

$$1/L = 1/d \tag{11}$$

i.e., $L = d$. The distance between dislocations decreases with the rising dislocation density. For simplicity, it can be assumed that the dislocations are distributed uniformly and hence the dislocation spacing can be given by [31]:

$$d = 1/\sqrt{\rho} \tag{12}$$

By combining Eqs. (2), (9), (11) and (12), the rate of dislocation multiplication from the onset of DRX to stress peak can be represented as:

$$d\rho_m/d\varepsilon = \sigma/(\alpha GMb^2) \tag{13}$$

DRX nucleates at the initial grain boundaries or within the deformed and recovered structure. These nuclei then grow up and consume the deformed grains, resulting in a new grain structure with a low dislocation density [32]. The rate of dislocation annihilation after the occurrence of DRX can be expressed as [33]:

$$\frac{d\rho_a}{d\varepsilon} = -\frac{1}{\dot{\varepsilon}} \cdot \frac{3GV_m\beta\delta\rho^2}{ARTb} \cdot \left(\frac{\sigma}{G}\right)^p \cdot D_0 \cdot exp\left(-\frac{Q_s}{RT}\right) \tag{14}$$

where V_m denotes the molar volume, β the fraction parameter with the estimated value of 0.1-0.5 [34], δ the grain boundary thickness, A the material constant and Q_s the self-diffusivity along a grain boundary, and p ranges from 1.5 to 2.0 for most metals and alloys [35, 36].

With substituting Eqs. (13) and (14) into Eq. (3), the strain hardening rate after DRX onset until stress peak can be written as:

$$\theta_2 = \frac{d\sigma}{d\rho} \cdot \frac{d\rho}{d\varepsilon} = \frac{\alpha GM}{2} - \frac{3v_m\beta\delta}{2ARTbG^{P-1}} \cdot D_0 \cdot exp\left(-\frac{Q_s}{RT}\right) \cdot \frac{1}{(\alpha GMb)^2} \cdot \frac{\sigma^{3+p}}{\dot{\varepsilon}} \tag{15}$$

When it comes to the critical condition, Eq. (15) can be rewritten as:

$$\theta_c = \frac{\alpha GM}{2} - \frac{3v_m\beta\delta}{2ARTbG^{P-1}} \cdot D_0 \cdot exp\left(-\frac{Q_s}{RT}\right) \cdot \frac{1}{(\alpha GMb)^2} \cdot \frac{{\sigma_c}^{3+p}}{\dot{\varepsilon}} \tag{16}$$

The different relations are plotted in Fig. 5 with a linear fitting method and the fourth power of σ_c best fits the experiment data ($R^2 = 0.9520$ at 1140℃ and $R^2 = 0.9848$ at 1170℃). Thus, the relationship between the critical stress σ_c and strain rate $\dot{\varepsilon}$ may be represented by:

$$\dot{\varepsilon} \propto {\sigma_c}^4 \tag{17}$$

Moreover, p ranges from 1.5 to 2.0 as mentioned above and $p = 2.0$ is used for this case. With substituting of Eq. (17) and $p = 2.0$, Eq. (16) can be expressed as:

$$\theta_c = \frac{\alpha GM}{2} - \frac{3v_m\beta\delta}{2ARTbG^{P-1}} \cdot D_0 \cdot exp\left(-\frac{Q_s}{RT}\right) \cdot \frac{1}{(\alpha GMb)^2} \cdot a \cdot \sigma_c \quad (18)$$

i.e., $\theta_c = A_1 \cdot \sigma_c + A_2$ (19)

where a is the proportionality coefficient, $A_1 = -\frac{3v_m\beta\delta}{2ARTbG^{P-1}} \cdot D_0 \cdot \exp\left(-\frac{Q_s}{RT}\right) \cdot \frac{1}{(\alpha GMb)^2} \cdot a$; $A_2 = \alpha GM/2$. A_1 and A_2 are independent of strain rate and depend on deformation temperature only. Therefore, the linear relationship between the critical strain hardening rate and the critical stress does exist at a given deformation temperature. Correspondingly, it is reasonable to determine this relationship by using a linear fit method as follows:

$$\theta_c = \begin{cases} 2.87\sigma_c + 741.45, & T = 1140℃ \\ 3.97\sigma_c + 6.43, & T = 1170℃ \end{cases} \quad (20)$$

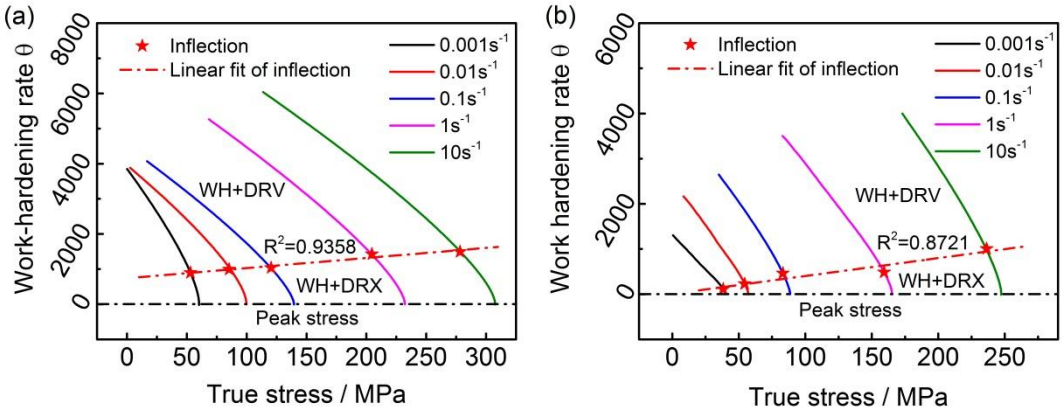

Fig. 4 Strain hardening rate versus true stress: (a) 1140℃, (b) 1170℃.

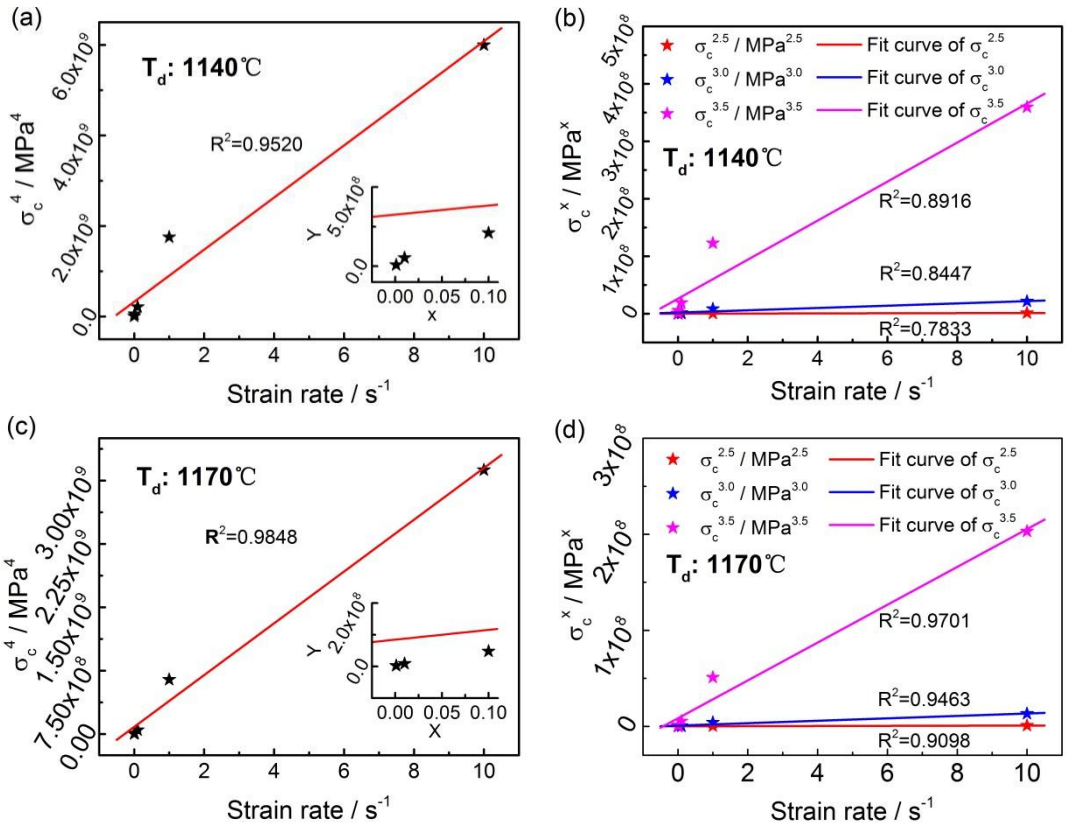

Fig. 5 Relations between the critical stress and strain rate.

As shown in Fig. 6, it is also recognized that the critical stress and strain can be estimated from the peak stress and strain by using a linear model as follows [37]:

$$\sigma_c = \begin{cases} 0.91\sigma_p - 4.763, & T = 1140℃ \\ 0.95\sigma_p - 0.348, & T = 1170℃ \end{cases} \tag{21}$$

$$\varepsilon_c = \begin{cases} 0.4420\varepsilon_p + 0.0057, & T = 1140℃ \\ 0.7479\varepsilon_p - 0.0117, & T = 1170℃ \end{cases} \tag{22}$$

Based on Eqs. (20), (21) and (22), the critical strain, stress and strain hardening rate can be all determined from the peak strain and stress directly.

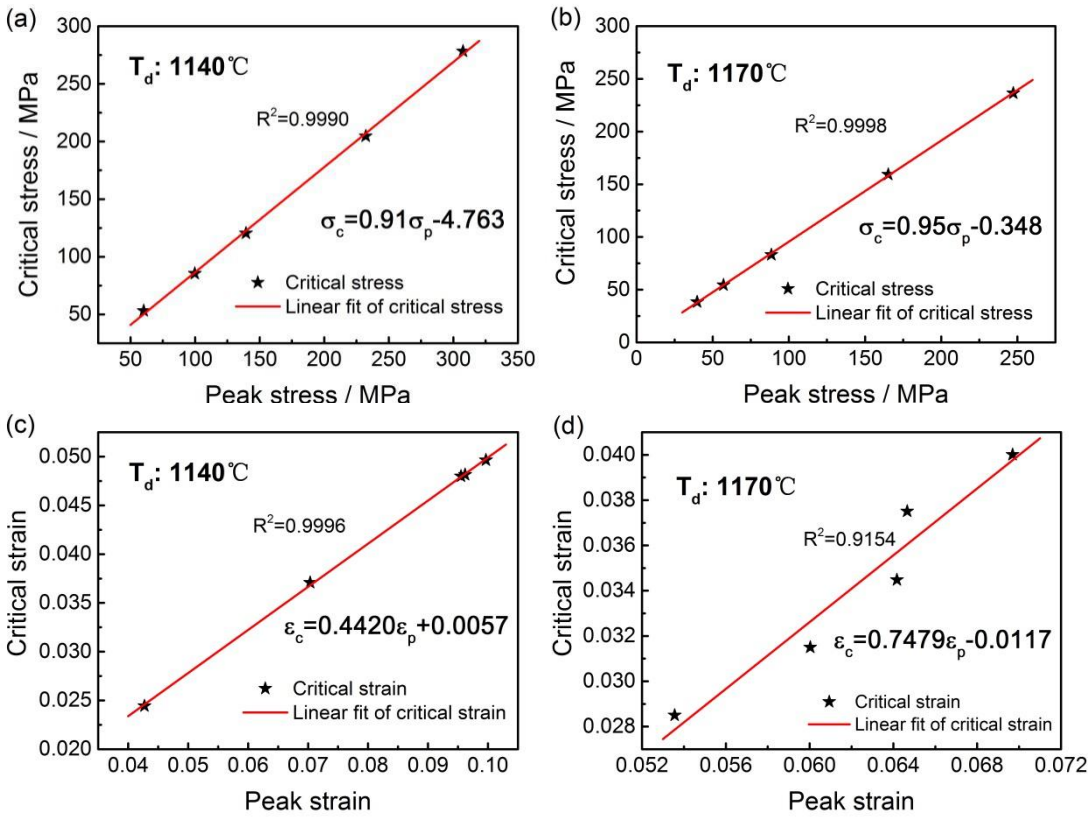

Fig. 6 Critical stress versus peak stress: (a) 1140℃, (b) 1170℃; critical strain versus peak strain: (c) 1140℃, (d) 1170℃.

3.2 Microstructure evolution

3.2.1 Effects of deformation parameters on microstructure

As mentioned in Section 3.1.1, all samples cracked severely for strong localization of strain when deformed below 1080℃ with the strain rate range of 0.001 to 10 s^{-1} and at the temperature range of 1050 to 1170℃ with the strain rate of 10 s^{-1}. No crack was detected when the samples were deformed above 1110℃ with the strain rate range of 0.001 to 1 s^{-1}. This temperature and strain rate range is exactly the focus in the present work.

Fig. 7 shows the microstructures of columnar structures deformed at different

temperatures and strain rates with a true stain of 0.69. Typical necklace structures occurred when the samples were deformed at 1110℃, especially for the samples deformed at low strain rates (Fig. 7(a) and (b)), indicating the occurrence of DRX at 1110℃. All DRX nuclei observed by OM were located at the original high-angle grain boundaries (HAGBs) instead of deformation band and the inside of the original grains, which was very different from the behavior observed in the same alloy with equiaxed grains [14]. For a given slip system, it would be first activated in the grains or subgrains with the highest Schmid factor (SF) during the deformation of metal materials [38]. Every columnar grain or subgrain in the columnar structure used in this work had a similar SF due to the strong texture. However, the equiaxed structure had an almost random distribution of SF in different grains or subgrains. Grains or subgrains with the highest SF were first deformed during deformation process and DRX nuclei tended to occur at these zones (deformation bands) correspondingly. As for the columnar structure used in this work, the deformation was more uniform by comparison with the equiaxed structure which had an almost random distribution of SF. Therefore the local deformation bands were observed rarely within the columnar grains and HAGBs was the preferred sites for DRX nucleation naturally. DRX has completed for the samples deformed above 1140℃, except for those deformed with higher strain rates ($\geq 0.1\ s^{-1}$), indicating the limitation of time in the microstructure evolution. The new DRX grain size of the samples evolved at the strain rate of 0.001 and 0.01 s^{-1} were counted to be 142 and 58 μm, respectively. No original grains are found under these two deformation conditions (Fig. 7(c) and (d)). However, the obviously deformed grains and DRX bands along the HAGBs were observed for the samples deformed above 1140℃ with the strain rate higher than 0.1 s^{-1} (Fig. 7(e)). HAGBs were believed to play an important role during the microstructure evolution for the studied material. The necklace structures mentioned before was also a strong evidence for this conclusion (Fig. 7(a) and (b)). It is worth noting that some new DRX grains occurred

inside the deformed grains, which was related to the defects or special substructures within deformed grains [39]. For the samples deformed at 1170℃, the solution of γ` phase is an important factor that affected the microstructure evolution. γ` phase hindered the movement of dislocations, subgrain boundaries and grain boundaries, which strongly influenced the behaviors of microstructure evolution. All grains that evolved at 1170℃ were coarser than those evolved at 1140℃ due to the absence of γ` phase, as shown in Fig. 7(d), (e), (f) and (g). Elevated deformation temperature and decreasing strain rate also accelerated DRX process and resulted in the increase of new DRX grain size and its volume fraction correspondingly. Moreover, more new DRX grains could be detected inside the original grains that deformed at 1170℃ by comparison with those deformed at 1140℃, indicating that the importance of intragranular nucleation increased with the deformation temperature.

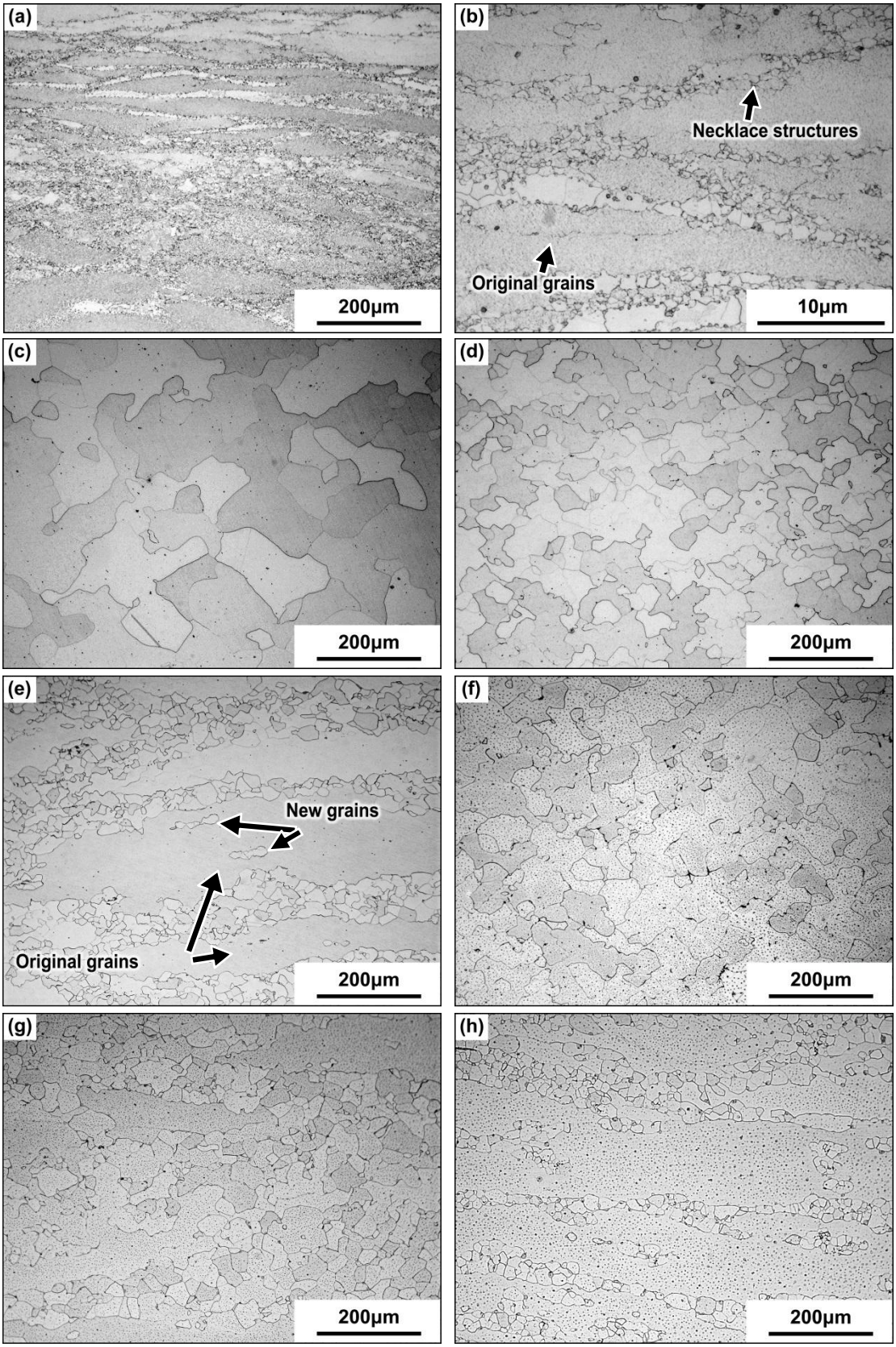

Fig. 7 Typical microstructures of the columnar grains after hot processing with different

parameters: (a) (b) 1110℃/0.001 s^{-1}, (c) 1140℃/0.001 s^{-1}, (d) 1140℃/0.01 s^{-1}, (e) 1140℃/0.1 s^{-1}, (f) 1170℃/0.01 s^{-1}, (g) 1170℃/0.1 s^{-1}, (h) 1170℃/1 s^{-1}.

3.2.2 DRX nucleation and evolution

Fig.8 shows the orientation imaging microscopy maps of the studied superalloy deformed at 1140℃. By comparison Figs. 1(b) with 8(a), it was observed that the columnar grains were elongated severely when deformed at 1 s^{-1} with a strain of 0.69. Grain boundaries (GBs) became serrated due to the deformation compatibility between adjacent grains and fine DRX grains were detected along these boundaries. The serrated grain boundaries usually possess high local orientation or strain gradients, and thus can be the potential sites for discontinuous-DRX (DDRX) nucleation through grain boundary bulging [40]. Original GBs migrated locally due to the energy difference between adjacent grains during deformation. Meanwhile, the orientation near the serrated grain boundaries changed gradually. Subsequently, the low angle grain boundaries occurred due to dislocation rearrangement and finally develop into HAGBs (marked by a black arrow in Fig. 8(a)). When HAGBs here were enough to form a closed loop, a fine DRX grain occurred and finally grew into a new grain if the deformation time was enough (marked by a white arrow in Fig. 8(a)). Obviously, DDRX occurred under this deformation condition, which was characterized by grain boundary bulging, but was restrained by deformation time. Although high strain rate produced high dislocation density and provided more deformation stored energy correspondingly, the deformation time at high strain rate restrained the evolution of DRX nuclei and finally influenced the microstructure of this alloy. DRX became easier to develop when strain rate decreased. At the strain rate of 0.01 s^{-1}, the serrated grain boundaries were easier to be detected. The nuclei grew by consuming the deformed grains and finally replaced the

deformed grains (Fig. 8(d) and (e)).

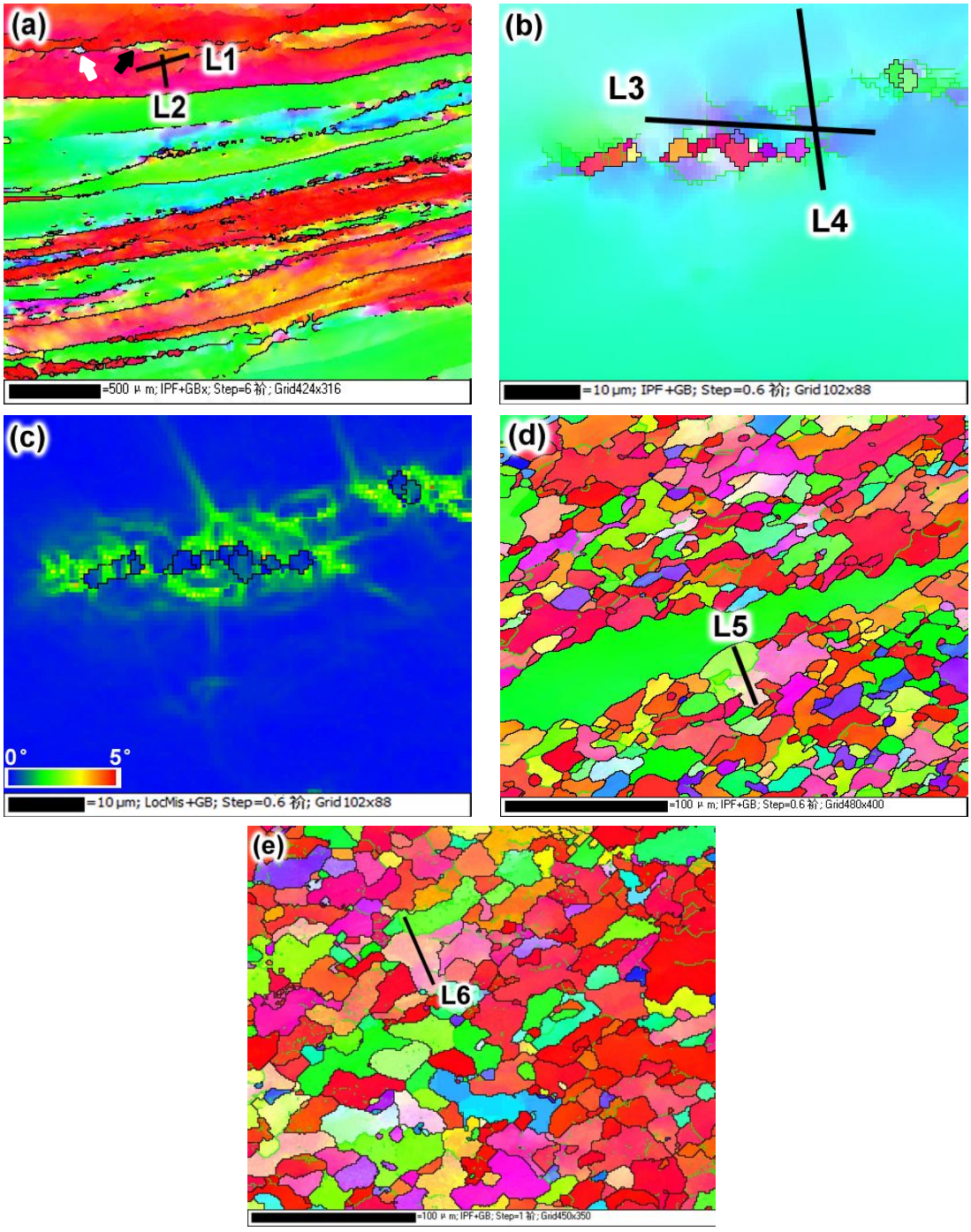

Fig. 8 Orientation imaging microscopy (OIM) maps of columnar structures deformed at 1140℃: (a) $\dot{\varepsilon}=1\ s^{-1}/\varepsilon=0.69$, (b) refined analysis within original grains of (a), (c) kernel average misorientation (KAM) map for (b), (d) $\dot{\varepsilon}=0.01\ s^{-1}/\varepsilon=0.36$, and (e) $\dot{\varepsilon}=0.01\ s^{-1}/\varepsilon=0.69$.

It is worth noting that some new fine grains could be observed within the original grains (Fig. 8(a)), which might be attributed to the subgrain rotation, shear bands, twins, second-phase particles and so on. The misorientation profile along the lines marked in Fig. 8 is plotted in Fig. 9. As shown in Fig. 9(a) and (b), the point-to-origin (cumulative) misorientation was easily to exceed 10° along the marked lines, particularly along the direction perpendicular to length direction of the columnar grains. The strain gradients in the deformation might lead to a subgrain rotation and finally generated DRX nuclei. Refined EBSD analysis using small step size (0.6 μm) within the original grains was conducted to verify this possibility (Fig. 8(b)). Misorientation profile showed that the point-to-origin misorientation around DRX nuclei within original grains exceeded 10° at a distance range from 0 to 12 μm (Fig. 9(c) and (d)). Fig. 8(c) is the KAM map corresponding to Fig. 8(b). High KAM values were observed around the new DRX nuclei within the deformed grains. While the new grains were featured by very low KAM values due to DRX. This is consistent with the conclusion from misorientation profiles. In addition, no shear band, twin or second-phase particle was detected around here. It means that the continuous-DRX (CDRX) nucleation mechanism characterized by progressive subgrain rotation took place within the deformed grains [41]. Similar subgrain rotation was observed in samples that deformed at a lower strain rate with different strain (ε=0.36 and ε=0.69). L5 was marked within a special grain, where the DRX process almost completed. This grain was divided into two different subgrains (green part and pink part) by a subgrain boundary with the misorientation angle of 7°, as shown in Fig. 8(d). Fig. 9(e) indicates that the point-to-point misorientation could not exceed 2°within the green part and pink part. It means that these two parts seldom possessed substructure, i.e. two dislocation-free DRX grains almost occurred. It is reasonable to deduce that the boundary with the misorientation angle of 7° would develop into a grain boundary

(>15°) through subgrain rotation with the increasing strain. This deduction was verified by the misorientation profile from the sample that deformed at same temperature and strain rate with a strain of 0.69 (Figs. 8(e) and 9(f)). A similar grain was divided into two subgrains by a subgrain boundary with misorientation angle of 14° here. Therefore, CDRX also played an important part in the microstructure evolution of the columnar structures.

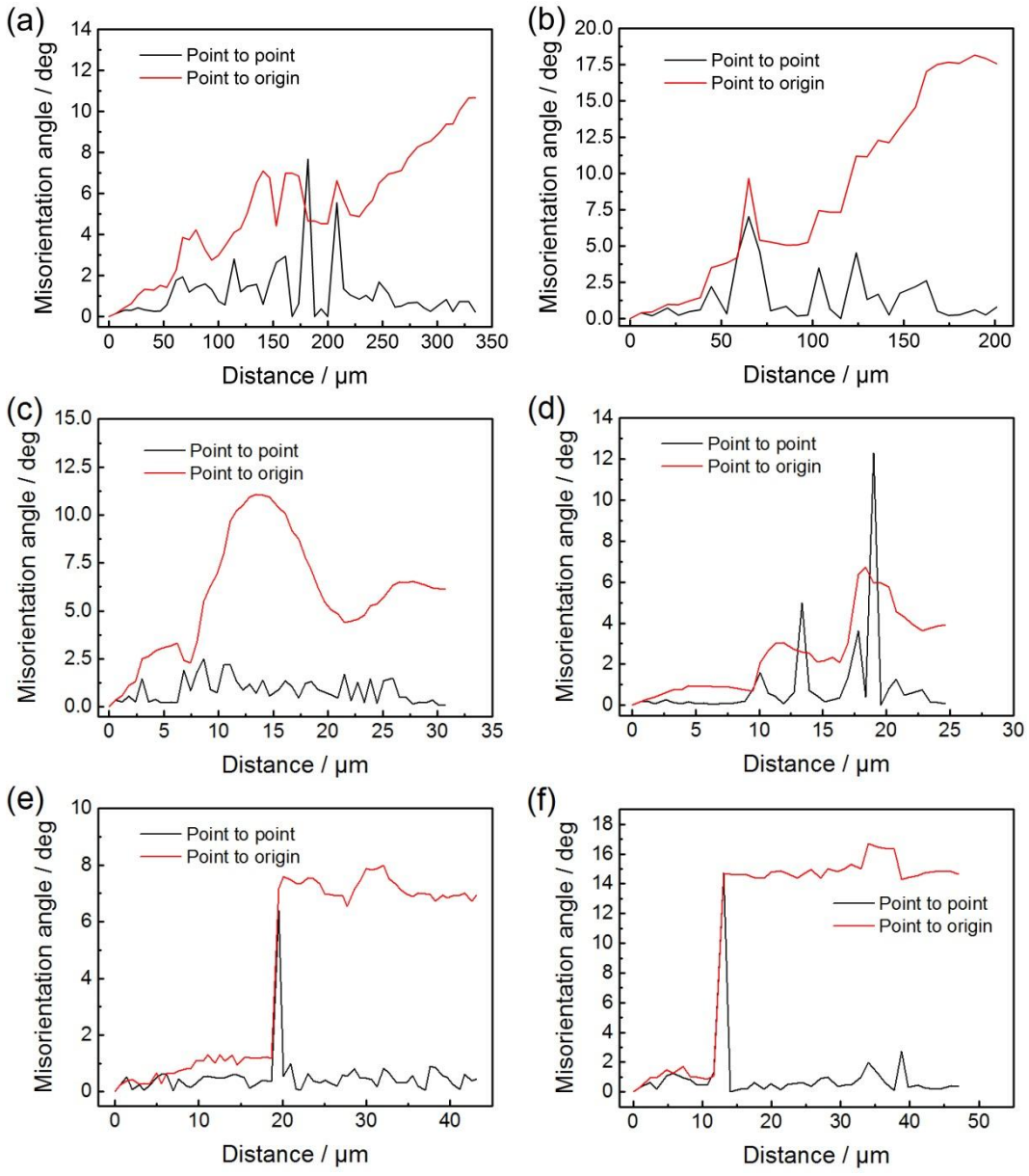

Fig. 9 Misorientation profiles along the lines marked in Fig. 8: (a) L1, (b) L2, (c) L3, (d) L4, (e) L5 and (f) L6.

Fig. 10 shows the orientation microscopy image maps of the sample deformed at 1170℃ and 1 s^{-1} with strain of 0.69. The dynamic recrystallization degree obviously increases by comparison with that at 1140℃ and 1 s^{-1} (Fig. 8(a)). Although the strain rate was high and hence restrains the DRX process, the increased temperature provided more driven force for grain boundary migration and accelerated the DRX process in such a way. It was found that most of the fine DRX grains were located at the initial grain boundaries, which was similar to that at 1140℃. The fraction of fine grains within the deformed grains increased evidently, which was related to the substructure inside the deformed grains. In order to analyze the substructure development within the deformed grain at 1170℃ and 1 s^{-1}, the local (point-to-point) and cumulative (point-to-origin) misorientations were calculated. The misorientation profile across the deformed grains (lined in Fig. 10) is given in Fig. 11. It was found that the cumulative misorientation easily exceeded 15° across the deformed grain (Fig. 10(a)). It indicated that the progressive subgrain rotation developed well [42], which was the characteristic of CDRX nucleation [41]. When deformed at this condition, subgrains occurred by DRV and the local orientation deviated from the initial orientation gradually due to subgrain rotation. The misorientation between the subgrain and the initial grain accumulated continuously with the increase of strain, and finally the subgrain boundary developed into grain boundary, i.e., a new grain occurred. Therefore, intracrystalline nucleation played an important role when the deformation was performed at this condition.

Fig. 11 shows that several sharp peaks appeared in the local (point-to-point) misorientation curves both in Fig. 11(a) and (b), revealing that the deformed grain was

divided into different orientation bands by some boundaries [17]. These boundaries accommodated the lattice misorientations and ensured the plastic strain compatibility between adjacent grains by shearing of the different slip system combinations and were thus named as the geometrically necessary boundaries (GNBs) [43-45]. Moreover, it was observed that the point-to-origin misorientation profiles did not keep cumulating along the lines marked in Fig. 10. The point-to-origin misorientation of L7 quickly cumulated at the distance range from 0 to 135 μm. Then an obvious misorientation jump occurred because a geometrically necessary boundary divided the deformed grain. The accumulation slowed down after this location and then a relative steady but fluctuating stage occurred. Subsequently, the curve decreased until another fluctuating stage at the distance range from 886 to 1057 μm. Cumulative misorientation fluctuated more obviously along L8 (Fig. 11(b)). The fluctuating lattice orientations were related to the formation of parallel microbands. It was the alternating orientation in the microbands that weakened the misorientation accumulation across the deformed grains [41].

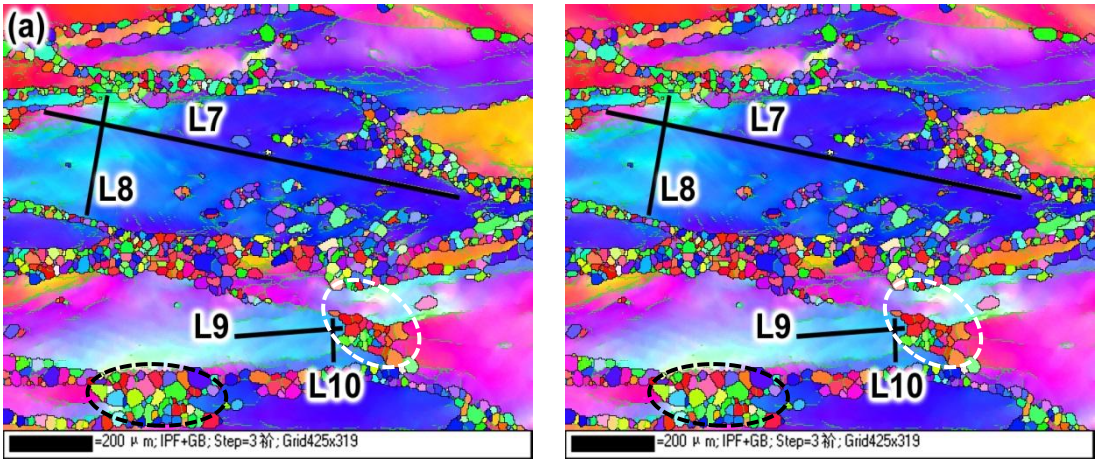

Fig. 10 OIM maps of the columnar structures deformed to ε=0.69 at 1170°C and strain rate of 1 s^{-1} with different loading directions: (a) perpendicular to the columnar-grain direction; (b) parallel to the columnar-grain direction.

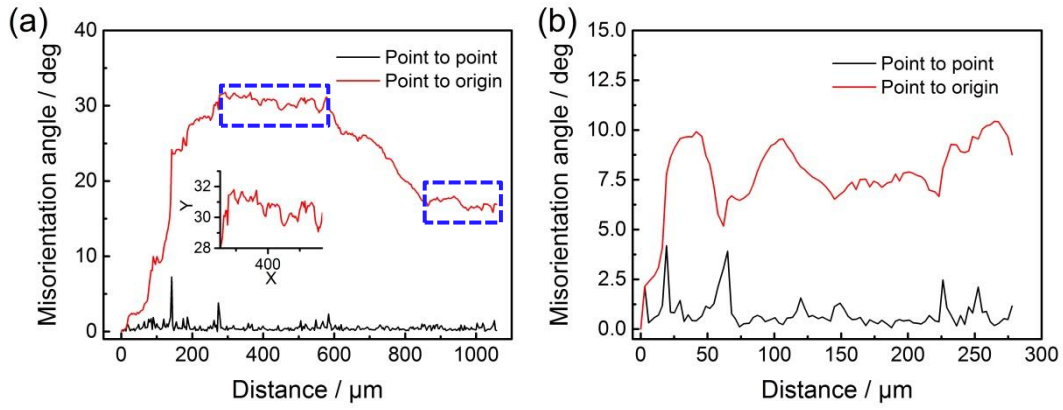

Fig. 11 Misorientation profiles along the lines marked in Fig. 10: (a) L7 and (b) L8.

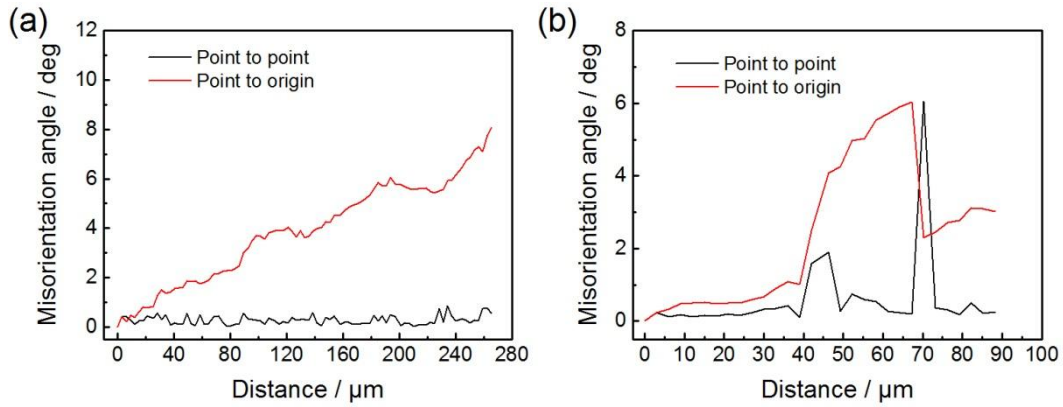

Fig. 12 Misorientation profiles along the lines marked in Fig. 10: (a) L9 and (b) L10.

Due to a special cutting direction, the grain boundaries parallel to loading direction can be observed easily in Fig. 10. It was found that the fine DRX grains appeared along the boundaries parallel to loading direction more easily (circled by dash-dotted line in Fig. 10(a)), which was very different from fine-grain wrought superalloy. Similar nucleation preference was also observed in the samples deformed along the columnar-grain direction (Fig. 10(b)). As discussed above, DDRX and CDRX both played an important role during the deformation process of the columnar structures. However, the misorientation profiles were hard to exceed 10° near the grain boundaries along the loading direction, as shown in Fig. 12. It means that

the CDRX did not take place near this type of grain boundaries. Therefore, the DDRX was responsible for this heterogeneous distribution of the new fine DRX grains.

3.2.3 Misorientation angle evolution

Fig. 13 illustrated the misorientation angle distribution of the columnar structures under different deformation conditions. The correlated misorientation plot presents the misorientation data between neighboring points in a map. The uncorrelated misorientation plot data shows the misorientation between randomly chosen points in the data set, and the random curve means the random distribution of misorientation for a purely random texture. It was found that both the correlated and the uncorrelated misorientation plots were very different from the random one and from each other in all deformation conditions involved here. A large number of boundaries with angle below 5° existed in all deformation conditions and the frequency decreased with the decrease of strain rate and the increase of deformation temperature. It was consistent with the tendency of the degree of DRX discussed above. The limited time at the high strain rate restrained DRX and a large number of boundaries with misorientations below 5° hence survived. However, the decreasing strain rate and elevating deformation temperature respectively provided a relevant sufficient time and enough driven force for grain boundary migration and subgrain rotation. Therefore, low angle subgrain boundaries (LAGBs) developed into HAGBs more easily and the frequency of boundaries with misorientation angle below 5° decreased correspondingly. It could also be verified by the change of average misorientation angle demonstrated in Fig. 13. Therefore, the misorientation angle evolution is sensitive to the deformation condition and has a strong connection with the microstructure evolution discussed above. As for the difference between

the uncorrelated misorientation and the random misorientation, the strong fiber texture of initial columnar grains should be blamed.

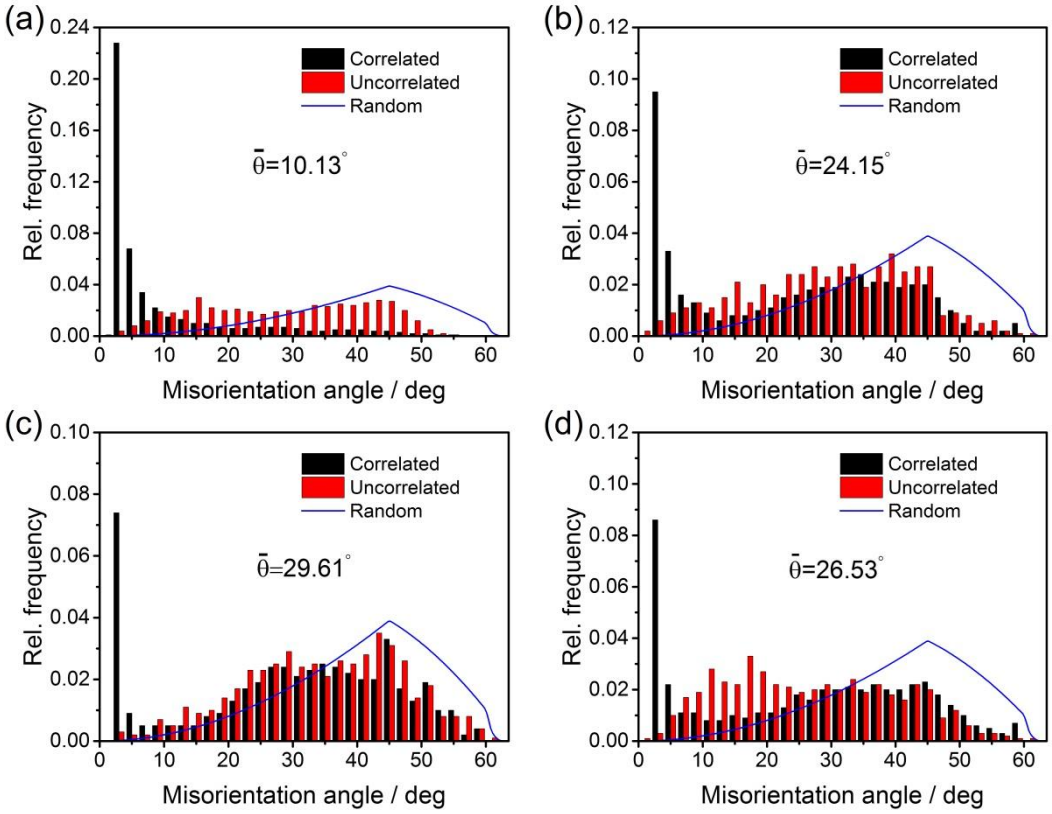

Fig. 13 Misorientation angle distributions of the columnar structures at a constant strain of 0.69: (a) 1140℃/1 s^{-1}, (b) 1140℃/0.1 s^{-1}, (c) 1140℃/0.01 s^{-1} and (d) 1170℃/1 s^{-1}.

4. Conclusions

In view of the difference between casting columnar and wrought equiaxed structures, a nickel-based superalloy ingot with columnar grains was hot deformed at a temperature range of 1050-1170℃ and a strain rate range of 0.001-10 s^{-1}. The DRX mechanisms and microstructure evolution were studied particularly. Several conclusions derived from the work are summarized in the following:

(1) A linear relationship between the critical strain hardening rate and the critical stress was verified at a given deformation temperature. On this basis, the critical stress and strain, as well as the critical strain hardening rate can be calculated from the peak stress and strain directly, which can be used to predict the critical condition of DRX efficiently.

(2) DDRX and CDRX both played an important role in microstructure evolution for the columnar grains studied in this research. For the coarse columnar grains, the DRX nuclei occur at the serrated grain boundaries through grain boundary bulging firstly (DDRX). Subsequently, the continuous misorientation accumulation leads to orientation bands and the subgrain rotation, which accelerates the nucleation within the deformed grains (CDRX).

(3) DRX nucleation of columnar structures exhibits more dependence on grain boundaries by comparison with that in equiaxed structures. The DRX nuclei prefer the grain boundaries that are parallel to the loading direction and hence leading to the heterogeneous distribution of the new fine DRX grains. DDRX is considered to be the main nucleation mechanism at these special grain boundaries.

(4) The misorientation angle evolution is sensitive to the deformation conditions and has a strong connection with microstructure evolution. The average misorientations under various deformation conditions vary with the DRX degree in the same tendency.

Acknowledgements

The work was financially supported by the National Natural Science Foundation of China (Grant No. 51775440) and Fundamental Research Funds for the Central Universities (Grant No. 3102018ZY005).

Data availability

The raw/processed data required to reproduce these findings cannot be shared at this time as the data also forms part of an ongoing study.

References

[1] S.L. Semiatin, D.S. Weaver, R.C. Kramb, P.N. Fagin, M.G. Glavicic, R.L. Goetz, N.D. Frey, M.M. Antony, Deformation and recrystallization behavior during hot working of a coarse-grain, nickel-base superalloy ingot material, Metall. Mater. Trans. A 35(2) (2004) 679-693, https://doi.org/10.1007/s11661-004-0379-y.

[2] Y.Q. Ning, B.C. Xie, H. Li, M.W. Fu, Dynamic recrystallization of wrought-solidified-wrought complex structure in Ni-based superalloys, Adv. Eng. Mater. 17(5) (2015) 648-655, https://doi.org/10.1002/adem.201400223.

[3] B.P. Kashyap, M.C. Chaturvedi, Activation energy for superplastic deformation of IN718 superalloy, Scripta Mater. 43(5) (2000) 429-433, https://doi.org/10.1016/S1359-6462(00)00453-X.

[4] B.M.B. Grant, E.M. Francis, J. Quinta da Fonseca, M.R. Daymond, M. Preuss, Deformation behaviour of an advanced nickel-based superalloy studied by neutron diffraction and electron microscopy, Acta Mater. 60(19) (2012) 6829-6841, https://doi.org/10.1016/j.actamat.2012.09.005.

[5] Y. Yuan, Y.F. Gu, T. Osada, Z.H. Zhong, T. Yokokawa, H. Harada, Deformation mechanisms in a new disc superalloy at low and intermediate temperatures, Scripta Mater. 67(2) (2012) 137-140, https://doi.org/10.1016/j.scriptamat.2012.03.042.

[6] B. Tian, C. Lind, E. Schafler, O. Paris, Evolution of microstructures during dynamic recrystallization and dynamic recovery in hot deformed Nimonic 80a, Mater. Sci. Eng. A 367(1) (2004) 198-204, https://doi.org/10.1016/j.msea.2003.10.226.

[7] H. Jiang, L. Yang, J. Dong, M. Zhang, Z. Yao, The recrystallization model and microstructure prediction of alloy 690 during hot deformation, Mater. Des. 104 (2016) 162-173, https://doi.org/10.1016/j.matdes.2016.05.033.

[8] Y.H. Liu, Y.Q. Ning, X.M. Yang, Z.K. Yao, H.Z. Guo, Effect of temperature and strain rate on the workability of FGH4096 superalloy in hot deformation, Mater. Des. 95 (2016) 669-676,

https://doi.org/10.1016/j.matdes.2016.01.032.

[9] Y.C. Lin, X.M. Chen, A critical review of experimental results and constitutive descriptions for metals and alloys in hot working, Mater. Des. 32(4) (2011) 1733-1759, https://doi.org/10.1016/j.matdes.2010.11.048.

[10] A. Momeni, S.M. Abbasi, On the opposition of dynamic recrystallization and solute dragging in steels, J. Alloys Compd. 622 (2015) 318-326, https://doi.org/10.1016/j.jallcom.2014.09.197.

[11] I. Mejía, G. Altamirano, A. Bedolla-Jacuinde, J.M. Cabrera, Modeling of the hot flow behavior of advanced ultra-high strength steels (A-UHSS) microalloyed with boron, Mater. Sci. Eng. A 610 (2014) 116-125, https://doi.org/10.1016/j.msea.2014.04.105.

[12] S.P. Coryell, K.O. Findley, M.C. Mataya, E. Brown, Evolution of Microstructure and Texture During Hot Compression of a Ni-Fe-Cr Superalloy, Metall. Mater. Trans. A 43(2) (2012) 633-649, https://doi.org/10.1007/s11661-011-0889-3.

[13] K.K. Li, M.S. Chen, Y.C. Lin, W.Q. Yuan, Microstructural evolution of an aged Ni-based superalloy under two-stage hot compression with different strain rates, Mater. Des. 111 (2016) 344-352, https://doi.org/10.1016/j.matdes.2016.09.007.

[14] Q.Y. Yu, Z.H. Yao, J.X. Dong, Deformation and recrystallization behavior of a coarse-grain, nickel-base superalloy Udimet720Li ingot material, Mater. Charact. 107 (2015) 398-410, https://doi.org/10.1016/j.matchar.2015.07.035.

[15] D.X. Wen, Y.C. Lin, J. Chen, X.M. Chen, J.L. Zhang, Y.J. Liang, L.T. Li, Work-hardening behaviors of typical solution-treated and aged Ni-based superalloys during hot deformation, J. Alloys Compd. 618 (2015) 372-379, https://doi.org/10.1016/j.jallcom.2014.08.187.

[16] Y.C. Lin, M. Chen, J. Zhong, Effect of temperature and strain rate on the compressive deformation behavior of 42CrMo steel, J. Mater. Process. Tech. 205(1-3) (2008) 308-315, https://doi.org/10.1016/j.jmatprotec.2007.11.113.

[17] Y.C. Lin, X.Y. Wu, X.M. Chen, J. Chen, D.X. Wen, J.L. Zhang, L.T. Li, EBSD study of a hot deformed nickel-based superalloy, J. Alloys Compd. 640 (2015) 101-113, https://doi.org/10.1016/j.jallcom.2015.04.008.

[18] E. Dupin, A. Yanagida, J. Yanagimoto, Modeling static and dynamic dinetics of microstructure evolution in type 316 stainless steel, Steel Res. Int. 85(6) (2014) 1099-1108, https://doi.org/10.1002/srin.201300173.

[19] D. Samantaray, S. Mandal, M. Jayalakshmi, C.N. Athreya, A.K. Bhaduri, V. Subramanya Sarma, New insights into the relationship between dynamic softening phenomena and efficiency of hot working domains of a nitrogen enhanced 316L(N) stainless steel, Mater. Sci. Eng. A 598 (2014) 368-375,

http://dx.doi.org/10.1016/j.msea.2013.12.105.

[20] N. Bozzolo, N. Souaï, R.E. Logé, Evolution of microstructure and twin density during thermomechanical processing in a γ-γ` nickel-based superalloy, Acta Mater. 60(13-14) (2012) 5056-5066, https://doi.org/10.1016/j.actamat.2012.06.028.

[21] A.A. Guimaraes, J.J. Jonas, Recrystallization and aging effects associated with the high temperature deformation of Waspaloy and Inconel 718, Metall. Trans. A 12(9) (1981) 1655-1666, https://doi.org/10.1007/bf02643571.

[22] R.L. Goetz, S.L. Semiatin, The adiabatic correction factor for deformation heating during the uniaxial compression test, J. Mater. Eng. Perform. 10(6) (2001) 710-717, https://doi.org/10.1361/105994901770344593.

[23] A. Dehghan-Manshadi, M.R. Barnett, P.D. Hodgson, Recrystallization in AISI 304 austenitic stainless steel during and after hot deformation, Mater. Sci. Eng. A 485(1) (2008) 664-672, https://doi.org/10.1016/j.msea.2007.08.026.

[24] Y.Q. Ning, X. Luo, H.Q. Liang, H.Z. Guo, J.L. Zhang, K. Tan, Competition between dynamic recovery and recrystallization during hot deformation for TC18 titanium alloy, Mater. Sci. Eng. A 635 (2015) 77-85, https://doi.org/10.1016/j.msea.2015.03.071.

[25] J.R. Klepaczko, Physical-state variables — the key to constitutive modeling in dynamic plasticity, Nucl. Eng. Des. 127(1) (1991) 103-115, https://doi.org/10.1016/0029-5493(91)90043-H.

[26] H. Mecking, U.F. Kocks, Kinetics of flow and strain-hardening, Acta Mater. 29(11) (1981) 1865-1875, https://doi.org/10.1016/0001-6160(81)90112-7.

[27] F. Montheillet, O. Lurdos, G. Damamme, A grain scale approach for modeling steady-state discontinuous dynamic recrystallization, Acta Mater. 57(5) (2009) 1602-1612, https://doi.org/10.1016/j.actamat.2008.11.044.

[28] Y. Estrin, H. Mecking, A unified phenomenological description of work hardening and creep based on one-parameter models, Acta Mater. 32(1) (1984) 57-70, https://doi.org/10.1016/0001-6160(84)90202-5.

[29] F.J. Humphreys, M. Hatherly, Chapter 2 - The Deformed State, in: F.J. Humphreys, M. Hatherly (Eds.), Recrystallization and Related Annealing Phenomena (Second Edition), Elsevier, Oxford, 2004, pp. 11-14, https://doi.org/10.1016/B978-008044164-1/50006-2.

[30] Y. Estrin, H. Mecking, A unified phenomenological description of work-hardening and creep based on one-parameter models, Acta Mater. 32(1) (1984) 57-70, https://doi.org/10.1016/0001-6160(84)90202-5.

[31] E.I. Galindo-Nava, P.E.J. Rivera-Díaz-del-Castillo, A thermodynamic theory for dislocation cell formation and misorientation in metals, Acta Mater. 60(11) (2012) 4370-4378,

https://doi.org/10.1016/j.actamat.2012.05.003.

[32] F.J. Humphreys, M. Hatherly, Introduction, in: F.J. Humphreys, M. Hatherly (Eds.), Recrystallization and Related Annealing Phenomena (Second Edition), Elsevier, Oxford, 2004, pp. 1-10, https://doi.org/10.1016/B978-008044164-1/50005-0.

[33] Y.Q. Ning, B.C. Xie, C. Zhou, H.Q. Liang, M.W. Fu, Strain-rate sensitivity of powder metallurgy superalloys associated with steady-state DRX during hot compression process, Met. Mater. Int. 23(2) (2017) 350-358, https://doi.org/10.1007/s12540-017-6313-9.

[34] C.R. Hutchinson, H.S. Zurob, C.W. Sinclair, Y.J.M. Brechet, The comparative effectiveness of Nb solute and NbC precipitates at impeding grain-boundary motion in Nb steels, Scripta Mater. 59(6) (2008) 635-637, https://doi.org/10.1016/j.scriptamat.2008.05.036.

[35] H.J. McQueen, J.J. Jonas, Recovery and recrystallization during high temperature deformation, in: R.J. Arsenault (Ed.), Plastic deformation of materials, Academic Press, New York, San Francisco, London, 1975, pp. 393-493, https://doi.org/10.1016/B978-0-12-341806-7.50014-3.

[36] C.M. Sellars, Recrystallization of metals during hot deformation, Philos. T. R. Soc. A 288(1350) (1978) 147-158, https://doi.org/10.1098/rsta.1978.0010.

[37] H. Mirzadeh, A. Najafizadeh, Prediction of the critical conditions for initiation of dynamic recrystallization, Mater. Des. 31(3) (2010) 1174-1179, https://doi.org/10.1016/j.matdes.2009.09.038.

[38] G.X. Hu, X. Cai, Y.H. Rong, Fundamentals of materials science, Shanghai Jiao Tong University Press, Shanghai, 2010, pp. 172-191,

[39] L. Blaz, T. Sakai, J.J. Jonas, Effect of initial grain size on dynamic recrystallization of copper, Met. Sci. 17(12) (1983) 609-616, https://doi.org/10.1179/030634583790420448.

[40] P. Poelt, C. Sommitsch, S. Mitsche, M. Walter, Dynamic recrystallization of Ni-base alloys—Experimental results and comparisons with simulations, Mater. Sci. Eng. A 420(1) (2006) 306-314, https://doi.org/10.1016/j.msea.2006.01.076.

[41] S. Mandal, A.K. Bhaduri, V. Subramanya Sarma, A study on microstructural evolution and dynamic recrystallization during isothermal deformation of a Ti-modified austenitic stainless steel, Metall. Mater. Trans. A 42(4) (2011) 1062-1072, https://doi.org/10.1007/s11661-010-0517-7.

[42] Y. Wang, W.Z. Shao, L. Zhen, X.M. Zhang, Microstructure evolution during dynamic recrystallization of hot deformed superalloy 718, Mater. Sci. Eng. A 486(1) (2008) 321-332, https://doi.org/10.1016/j.msea.2007.09.008.

[43] V. Randle, N. Hansen, D.J. Jensen, The deformation behaviour of grain boundary regions in polycrystalline aluminium, Philos. Mag. A 73(2) (1996) 265-282, https://doi.org/10.1080/01418619608244382.

[44] D. Jorge-Badiola, A. Iza-Mendia, I. GutiÉRrez, Evaluation of intragranular misorientation parameters measured by EBSD in a hot worked austenitic stainless steel, J. Microsc. 228(3) (2007) 373-383, https://doi.org/10.1111/j.1365-2818.2007.01850.x.

[45] D. Jorge-Badiola, A. Iza-Mendia, I. Gutiérrez, Study by EBSD of the development of the substructure in a hot deformed 304 stainless steel, Mater. Sci. Eng. A 394(1) (2005) 445-454, https://doi.org/10.1016/j.msea.2004.11.049.